Coupling between plasticity and phase transition in shock- and ramp-compressed single-crystal iron

N. Amadou,[1,2,*] T. de Resseguier,[1] A. Dragon,[1] and E. Brambrink[3,4]
[1]*Institut P′. CNRS. ENSMA. Université de Poitiers, 86961 Futuroscope, France*
[2]*Département de Physique, Université Abdou Moumouni de Niamey, BP. 10662 Niamey, Niger*
[3]*LULI - CNRS, Ecole Polytechnique, CEA, Université Paris-Saclay, F-91128 Palaiseau cedex, France*
[4]*Sorbonne Universités, UPMC Université Paris 06, CNRS, place Jussieu, 75252 Paris cedex 05, France*

(Received 23 January 2018; revised manuscript received 14 June 2018; published 20 July 2018)

Molecular dynamics simulations have been used to investigate the coupling process between plasticity and structural phase transformation in single-crystal iron under both shock and ramp compressions. In both cases, iron was found to yield via twinning. Then, the onset of the bcc-hcp phase transformation was shown to be tightly dependent on the plasticity history through a hardening-like effect, which in some conditions may inhibit the nucleation of the hcp phase.

DOI: 10.1103/PhysRevB.98.024104

I. INTRODUCTION

Detailed understanding of the response of solid materials to both static and dynamic compression under extreme conditions is essential for materials science and a variety of applications. One typical example is iron. Indeed, being at the center of several technological applications, iron is also the main component of the core of terrestrial-like planets so that knowledge of its phase diagram is fundamental for predicting the internal structure and dynamics of such planets. Propagation of compressive waves in solid materials can cause irreversible deformation through various processes: plasticity, polymorphic transitions, melting, etc.

Thus, iron is known to undergo a structural phase transition at about 13 GPa from the ground-state body-centered cubic (bcc) structure (α phase) to the high-pressure hexagonal close-packed (hcp) structure (ε phase) [1–5]. Whether plasticity occurs before this phase transition is still unclear. Plastic deformation in polycrystalline iron was shown in early experimental work [2,6,7]. More recently, plasticity was reported in thin vapor deposited single crystal but not in thick melt-grown single crystal [8–10]. Atomistic molecular dynamic (MD) simulations have been extensively used to investigate these phenomena at the lattice level.

For iron, three interatomic potentials provide reasonable agreement with experiment: the Voter–Chen [11], the modified version of the Ackland potential [12,13] and the modified analytic embedded-atom-model reported in Ref. [14]. The first predicts the bcc-hcp transition under dynamic compression at around 15 GPa with no evidence of plasticity in the bcc phase, in both polycrystal and single crystal (with or without defects) [15–19]. The second potential was mainly applied to polycrystalline iron [20,21] which was found to plastically yield under dynamic compression at a pressure of about 10 GPa before the structural phase transformation around 23 GPa [20]. The plasticity mechanism was dominated by dislocations generated at grain boundaries. Finally, the third potential was applied to both single-crystal and polycrystalline iron under shock compression [14,22]. In the single crystal, plastic deformation was only observed for shock loading along the [110] crystallographic direction at around 17 GPa, plasticity being mediated by dislocation nucleation, propagation, and multiplication. The onset pressure of the structural phase transition was estimated to be 18.0, 22.3, and 23.8 GPa along the [001], [110], and [111] directions, respectively [14]. On the other hand, polycrystalline iron was found to yield around 8 to 9 GPa, prior to the structural phase transformation around 10 to 13 GPa depending on the shock strength. The plasticity, in this case, was mainly dominated by grain boundaries activities and intragranular processes (lattice compression and slip). It was found to contribute to the phase transition by two different coupling modes resulting in two different variants of transition products [22].

Thus, despite extensive research, the dynamic response of single-crystal iron to both shock and ramp compression, including the bcc-hcp phase transition, its kinetics, and its coupling with plasticity still remains an open issue.

II. METHOD AND COMPUTATIONAL DETAILS

In this paper, we use nonequilibrium molecular dynamics (NEMD) simulations to study the foregoing coupling between plasticity and phase transition in defect-free single-crystal iron. Toward this end, both shock and ramp compressions were performed and the sample responses were found to differ significantly. [001]-oriented single crystals containing up to 50 million atoms were simulated with the LAMMPS molecular dynamics code [23]. The interactions between atoms were modeled with the embedded atom model formalism [24,25]. The iron model was the modified version of the Ackland potential [13] to account for both plasticity and phase transformation. The samples were initially thermalized to 50 K and then compressed by driving an effective infinite-mass wall piston with an imposed velocity v along the z direction. Periodic boundary conditions were used for the transverse

*nourou.amadou@polytechnique.edu

directions. In the ramp-compression case the piston velocity was varied linearly from zero to its maximum during the first half of the compression time and then held constant at that maximum during the last half period.

The per-atom pressure tensor (or compressive stress) was computed following [26]

$$P_{i_{\alpha\beta}} V_a = m_i v_{i_\alpha} v_{i_\beta} + \frac{1}{2} \sum_j (r_{i_\alpha} F_{i_\beta} + r_{j_\alpha} F_{j_\beta}), \qquad (1)$$

where α and β take on values x, y, and z; m_i is the atomic mass, and V_a is the atomic volume. The first term of Eq. (1) represents the momentum flow of atom i while the last terms correspond to the virial due to the pairwise interaction of atom i situated at position r_i with atom j at position r_j. F_i and F_j are, respectively, forces on atom i and j while the latter sums over all neighbors of atom i. Then, the individual atomic volume was estimated by using the Voronoi tessellation method with the VORO++ package [27]. To trace the wave propagation, the macroscopic local thermodynamic and mechanical properties were evaluated within a spatial planar bin (of three lattice constant width) perpendicular to the wave-propagation direction, i.e., the z direction. Thus, the longitudinal pressure P_z along the wave-propagation direction, the mean pressure P_m, and shear stress were computed as P_{zz}, $\frac{1}{3}(P_{zz} + P_{yy} + P_{xx})$, and $\frac{1}{2}[P_{zz} - \frac{1}{2}(P_{xx} + P_{yy})]$ bin averages, respectively. Furthermore, the temperature was computed from the fluctuation of the atomic velocity $\overrightarrow{v}_i$ about the planar bin average velocity $\overrightarrow{v}$ by $\frac{3}{2} n k_B T = \frac{1}{2} m \sum_i (\overrightarrow{v}_i - \overrightarrow{v})^2$, where k_B and n are the Boltzmann constant and total number of atoms in bin respectively, and i sums over all atoms in the bin. This approach is considered to be the most useful definition of temperature in analyzing MD shock wave data [28].

Finally, a local structural analysis was performed by adaptive common neighbor analysis (CNA) and centrosymmetry as implemented in the OVITO software [29].

III. SHOCK COMPRESSION

When the compressive wave propagates from the piston through the material, various processes occur at the atomic level, which in return affect the local sound speed, thus modifying the wave profile.

This evolution of the wave structure is a rich, although indirect way to investigate plasticity and phase transitions in dynamic compression experiments; see, e.g., Refs. [2–5]. In Fig. 1 the sample is shock compressed to a P_z maximum of about 48 GPa ($P_m \approx 40$ GPa) with a piston velocity of 800 m/s. Snapshots of atoms with pressure distribution and local structural analysis at different times are shown in Fig. 1(a). Here, the atoms are colored according to the $P_m V_a$ value. Besides, the hcp atoms (detected by CNA analysis) and stacking faults (detected by centrosymmetry analysis) are colored in brown and violet, respectively (regardless of pressure). Spatial profiles of pressure, shear stress, and temperature are shown in Figs. 1(b)–1(d). In principle, in this case of shock-loaded iron, the wavefront is expected to split into three waves: an elastic precursor associated with elastic compression of the bcc phase, a shock sometimes referred to as the P_1 wave associated with plastic compression of that phase, and a slower shock called

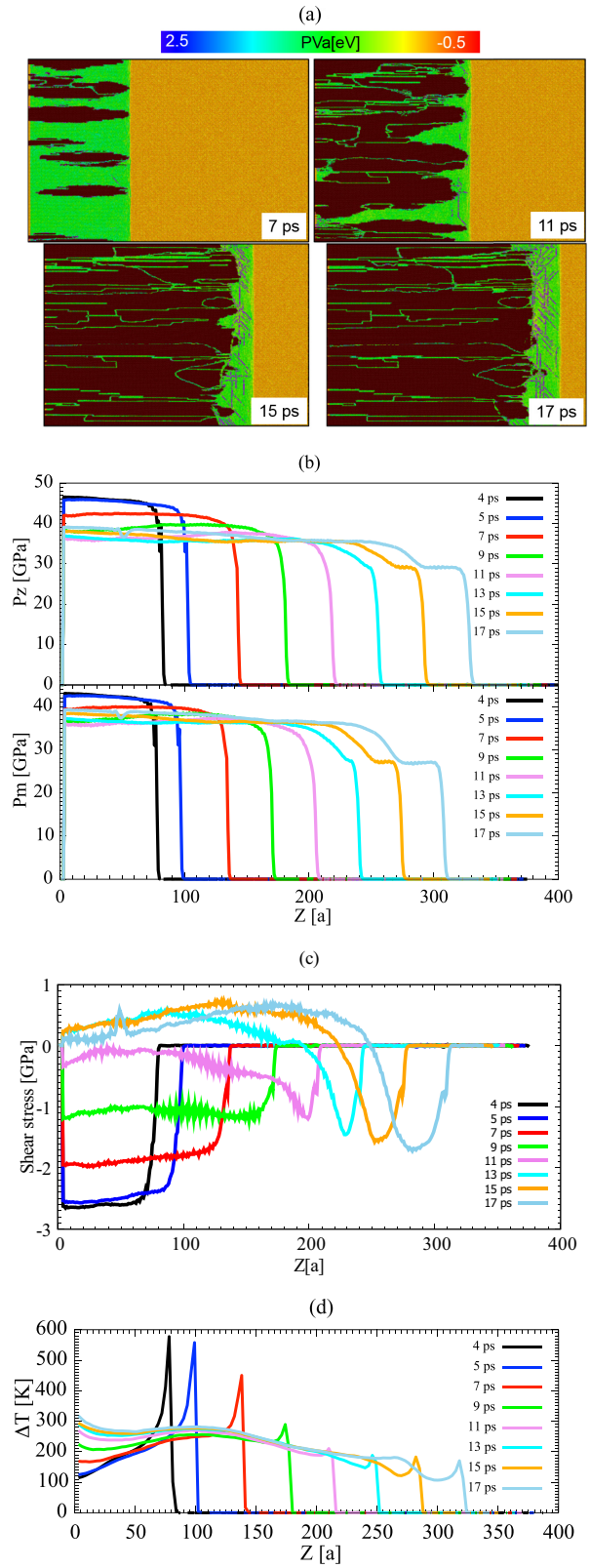

FIG. 1. Shock compression of single-crystal iron (piston velocity of 800 m/s). (a) Local structure analysis (CNA and centrosymmetry) with color scale showing pressure P_m and associated effects (plasticity, phase transition; for more details see text). (b)–(d) Spatial profiles of pressure [P_z; top of panel (b), and P_m; bottom of panel (b)], shear stress, and temperature, respectively.

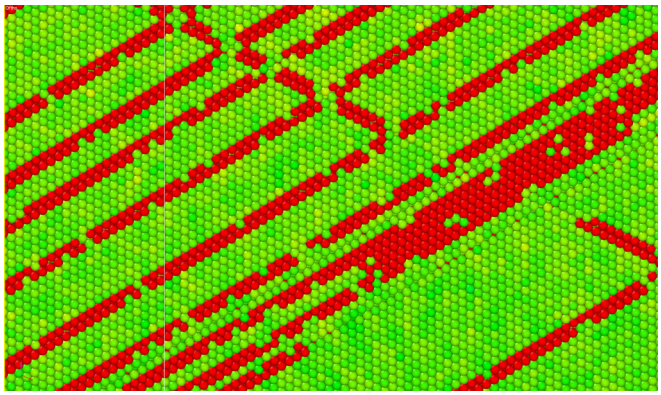

FIG. 2. Example of atom configuration in the $(1\bar{1}0)$ plane under ramp compression to P_z of 19 GPa ($P_m = 18$ GPa). Red lines are associated with twins.

the P_2 wave associated with the transition from the bcc phase to the hcp phase [2]. Here, the elastic wave is overdriven by the P_1 wave, so the compression front is observed to split into P_1 and P_2, separated by a plateau of increasing width [Fig. 1(b)]. The pressure P_z of about 29 GPa ($P_m \approx 26$ GPa) at the top of the P_1 wave corresponds to the onset pressure of the structural phase transformation. Although this value is greater than that at 13 GPa at equilibrium condition, it is consistent with what was found under dynamic laser compression [3,4] and with MD simulations of polycrystals [20,21].

Behind the P_1 wave and until the arrival of the P_2 wave, all atoms are still in the bcc phase but their coordination number increases from eight to ten [16]. The stacking faults associated with plastic compression were identified to be twins (see Fig. 2). This observation is consistent with previous MD simulations of plastic deformation in bcc material such as tantalum [30] and with the dynamic behavior of iron observed under both impact [31,32] and laser shock loading [7]. On the other hand, it contrasts with an absence of plasticity reported in other experiments [9] as well as in MD simulations that used the Voter–Chen potential [15,16,33], and with dislocation-based plasticity observed in polycrystalline iron in other MD simulations [20].

Computed profiles of the shear stress are shown in Fig. 1(c). At late times (e.g., 17 ps), two processes account for the shear relaxation: (i) the onset of the plastic deformation in the bcc phase bounds the maximum shear stress to about 1.3 GPa, then (ii) the extensive transformation into hcp phase produces a sharp drop of the shear stress and even its reversion, sometimes referred to as over-relaxation [15,16,33]. At earlier times (4 to 9 ps), both plastic deformation in the bcc phase and formation of the hcp phase are limited by kinetic effects, so that they do not yield significant relaxation while shear stress reaches 2 to 3 GPa.

This early, transient regime is characterized by sharp peaks in the temperature profiles [see Fig. 1(d)], qualitatively consistent with the strong dissipation expected in the steep compression front. Next, these peaks smooth down when the P1 and P2 waves separate, and the final temperature rise (behind the P2 wave) reaches an approximately steady value of about 280 K in good quantitative agreement with the iron SESAME 2140 table [34].

IV. RAMP COMPRESSION

In addition to shock loading, ramp compression has appeared as a successful technique to investigate the kinetics of phase transitions and their effects on wave dynamics [3,4,35]. In Fig. 3 the sample is ramp compressed from 0 to 800 m/s during 15 ps to a final P_z pressure of about 48 GPa ($P_m \approx$ 40 GPa) as the shock pressure in Fig. 1, then this pressure is maintained for another 15 ps. First, the sample is elastically compressed up to a pressure P_z of about 12 GPa ($P_m \approx 10$ GPa, yellow zone). Heating produced by this elastic compression remains very low; below 10 K [see Fig. 3(d)]. Then, yielding occurs as in the case of shock compression via twinning, which bounds the shear stress below about 1.5 GPa. In this plastic regime (green zone), the temperature increase remains moderate (about 20 to 30 K), which is consistent with the quasi-isentropic nature of ramp compression, until the wavefront steepens into a shock (after about 20 ps) accompanied by strong dissipation and significant heating. When the loading pressure P_z reaches 18 GPa (P_m about 17 GPa), the twins density starts to decrease, i.e., twins formed under moderate pressure are then removed upon further compression. This behavior is consistent with what was recently found experimentally for shock-induced twinning in tantalum [36], where the decrease in the twins density with increasing pressure was attributed to a transition to slip-dominated plasticity. However, in our computation, no significant dislocation activity was detected in the iron bcc phase; yet a hardening-like effect was observed with an increase in the shear stress [see Fig. 3(c)].

Such elastic stiffening of the bcc matrix leads to a confinement effect inhibiting the nucleation of the hcp embryos. Hence, the transition to hcp phase is not observed, unlike in former case of shock compression to the same pressure. This demonstrates that not only the maximum pressure determines the onset of the phase transformation but also the compression path and plasticity history.

V. DISCUSSION

The foregoing observations can be interpreted in the context of nucleation and growth theory of martensite phase transformation. As the bcc and hcp phases have different crystalline structures and specific volumes, the transformation is accompanied by dimensional changes. However, the changes in volume and shape cannot occur freely because of the rigidity of the surrounding matrix, and elastic strains induced [37]. Indeed, the total increase in Gibbs free energy associated with the formation of fully coherent embryos of hcp in the bcc matrix can be expressed as $\Delta G = -V\Delta G_v + A\gamma + V\Delta G_s$ where V is the volume of the nucleus, A is the surface area, and ΔG_v, ΔG_s, and γ are, respectively, the volume free-energy release, the strain energy, and the interfacial free energy [38]. Thus the strain energy reduces the effective driving force for the transformation [39]. For the embryos to be thermodynamically stable, they must reach a critical volume V_c which corresponds to a critical energy barrier (ΔG_c) given by the maximum of ΔG. For the flat spheroidal shape of embryos observed here, ΔG_c was shown to be proportional to $\mu^2\gamma^3/(\Delta G_v)^4$ where μ is the stiffness modulus of the matrix [38].

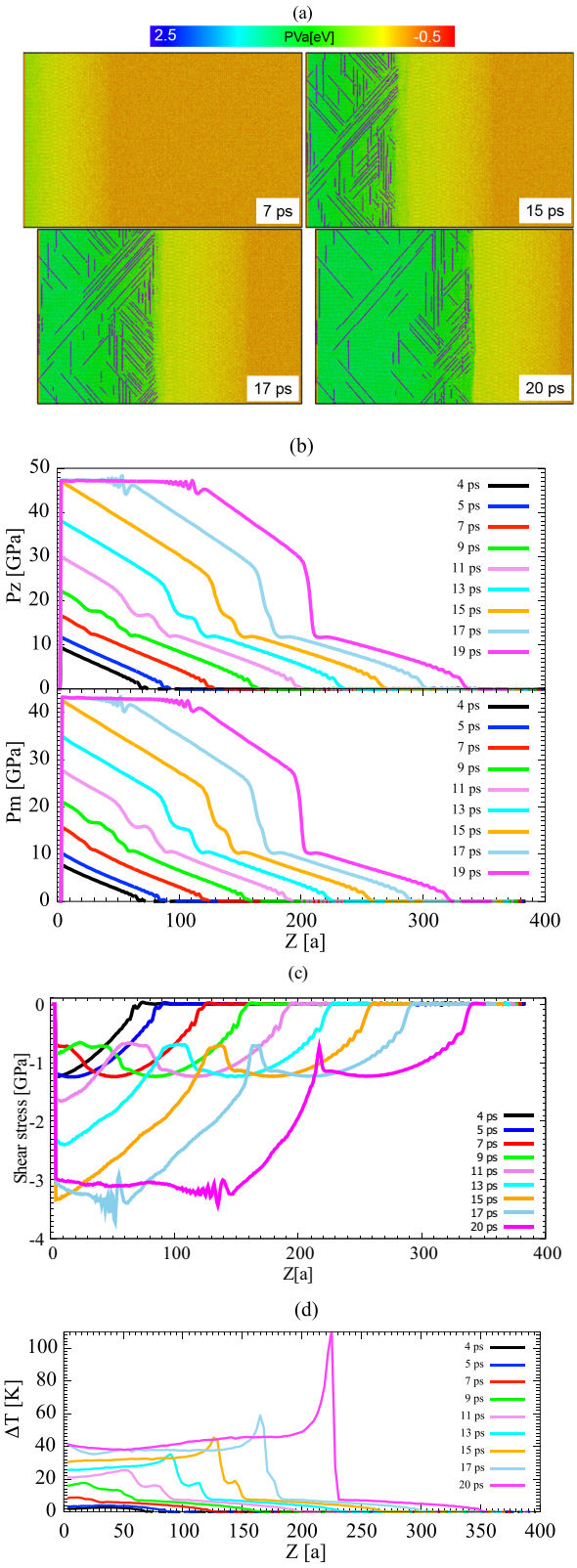

FIG. 3. Ramp compression of single-crystal iron (piston velocity of 800 m/s). (a) Local structure analysis (CNA and centrosymmetry) with color scale showing pressure P_m. (b)–(d) Spatial profiles of pressure [P_z; top of panel (b), and P_m; bottom of panel (b)], shear stress, and temperature, respectively. No structural phase transformation is observed (see text for details).

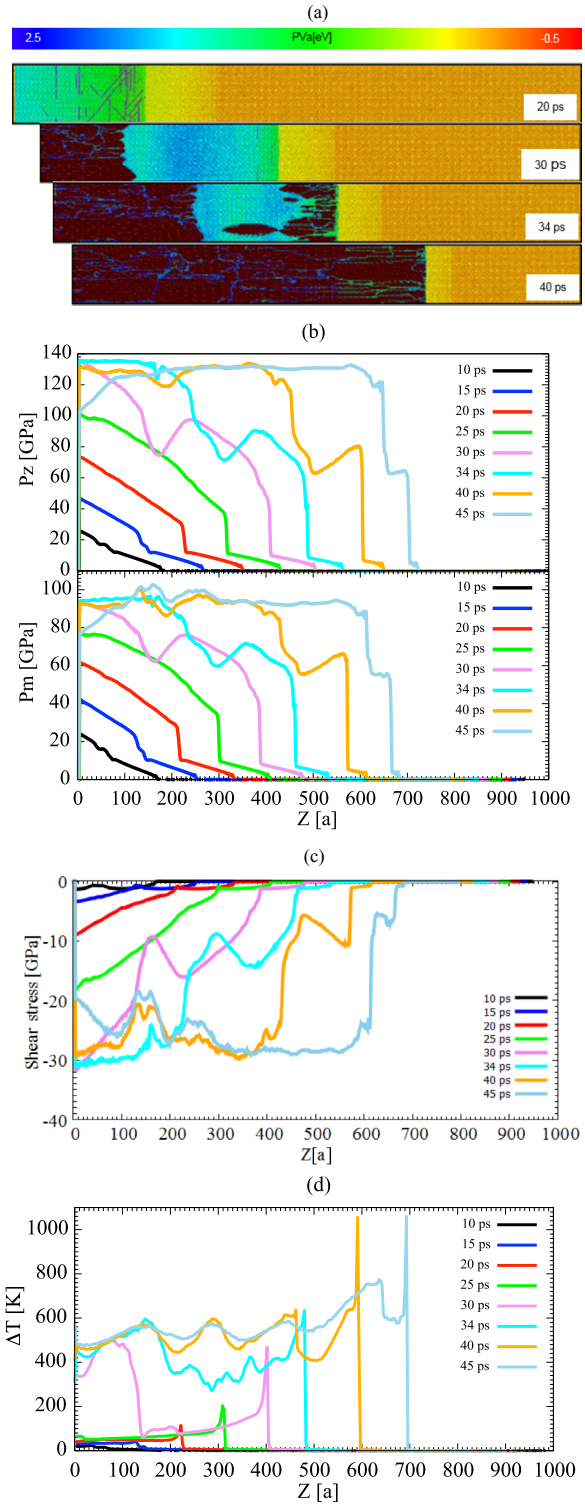

FIG. 4. Ramp compression of single-crystal iron (piston velocity of 1600 m/s): (a) local structure analysis (CNA and centrosymmetry) with color scale showing pressure P_m and brown zones showing hcp phase (for more details see text). (b)–(d) Spatial profiles of pressure [P_z; top of panel (b) and P_m; bottom of panel (b)], shear stress, and temperature, respectively. Two nucleation fronts are observed: one initiates near the piston side when ramp pressure reaches 140 GPa ($P_m \approx 95$ GPa) and another is behind the shock formed after ramp steepening. The full animated sequence is given in the supplementary material [40].

Based upon the above statements, the following scenarios emerge for nucleation and growth of the hcp phase. In the case of shock compression, the material is carried almost instantaneously from the thermodynamic stability conditions of the bcc phase to those of the hcp phase. The resulting driving force is high enough for hcp embryos to reach the critical volume almost instantly behind the shock front. Consequently, homogeneous nucleation is observed. On the other hand, in the case of ramp compression with the same maximum pressure, the material is continuously compressed by small pressure increments. The associated bulk driving force increment is small at each step. Therefore, no homogeneous nucleation is possible. Even heterogeneous nucleation is made difficult because of the matrix stiffness.

In order for the embryos to reach the critical volume, an increase in the bulk driving force is required. This drive can be provided in two different ways: (i) keep ramp compressing up to much higher pressure (by increasing the piston velocity) or (ii) let the ramp wave steepen during its propagation to evolve into a shock wave. In Fig. 4, the sample is ramp compressed to a higher P_z value of 140 GPa (P_m of about 100 GPa) with a final piston velocity of 1600 m/s and the same compression rate as in Fig. 3 (the ramp rising time is doubled, too). The first snapshots are very similar to those in Fig. 3. The sample deforms elastically, then yields around $P_z = 12$ GPa ($P_m = 10$ GPa). Further compression produces the hardening-like effect shown earlier, so that above P_z about 60 GPa ($P_m \approx 50$ GPa), the twin density is almost zero (blue color) while shear stresses increase to very high values of about 30 GPa. After 30 ps, the pressure at the top of the ramp reaches about 140 GPa ($P_m \approx 95$ GPa) in the left part of the sample, which is high enough for the onset of the phase transition despite previous hardening [drive type (i) mentioned above]. Meanwhile, the foot of the ramp has steepened into a shock during its propagation, so that, after 34 ps, the transformation initiates just behind this shock [drive type (ii) mentioned above, similar to the shock-loading case depicted in Fig. 1]. Both nucleation zones finally join after about 40 ps, giving rise to a single compression front progressively catching up with the elastic precursor.

This evolution of the wavefront has major effects in the temperature profiles shown in Fig. 4(d). Before 30 ps, the profiles are very similar to those in Fig. 3(d), with very small variation in the elastic regime and strong heating in the plastic wave, followed by cooling. The amplitude of the temperature peak logically increases while the plastic front steepens into a shock. At 30 ps, the occurrence of the phase transition in the left part of the target produces a new temperature increase. After 34 ps, similar heating is induced by the initiation of the phase transformation immediately behind the plastic front, which progressively overcomes cooling, until the two fronts catch up and temperature becomes roughly homogeneous in the compressed region, fluctuating around 530 K.

Finally, it can be noted that, while the initial, elastic response of the crystal is essentially one dimensional (longitudinal propagation of a planar front and uniform state along the transverse direction), a marked asymmetry appears behind the plastic wave (twinning in specific directions and locations, inhomogeneous onset of the phase transformation, oriented growth of the daughter phase). Thus, significant secondary anisotropy is induced in the system, associated with dissipation processes (plasticity and phase transition) which are accounted for in the computation.

VI. CONCLUSIONS

In summary, MD simulations have been used to investigate plasticity and polymorphic transformation in single-crystal iron. It was found that iron yields at about 12 GPa in the form of twinning in contrast with the absence of plasticity previously reported in some MD simulations. Thereafter, further ramp compression induces a progressive decrease in the twin density, accompanied by a hardening-like behavior leading to very high shear stresses and subsequent inhibition of the bcc-hcp phase transformation. This inhibition is overcome by either applying much higher pressure or shifting from ramp to shock compression (possibly after hydrodynamic steepening of the ramp wave). In the latter case, extensive phase transformation occurs just behind the shock front and induces a sharp relaxation of the shear stress. Thus, a strong coupling between plasticity and phase transformation has been shown and discussed. Such MD-based predictions might hopefully be compared with further experimental work involving, e.g., *in situ* probing of crystal structure under ultrafast compression, as available in x-ray free-electron laser (XFEL) facilities.

ACKNOWLEDGMENT

Computations were performed on the supercomputer facilities of the Mésocentre de calcul de Poitou Charentes (France).

[1] D. Bancroft, E. L. Peterson, and S. Minshall, J. Appl. Phys. **27**, 291 (1956).
[2] L. M. Barker and R. E. Hollenbach, J. Appl. Phys. **45**, 4872 (1974).
[3] R. F. Smith *et al.*, J. Appl. Phys. **114**, 223507 (2013).
[4] N. Amadou, T. de Resseguier, E. Brambrink, T. Vinci, A. Benuzzi-Mounaix, G. Huser, G. Morard, F. Guyot, K. Miyanishi, N. Ozaki, R. Kodama, and M. Koenig, Phys. Rev. B **93**, 214108 (2016).
[5] N. Amadou, E. Brambrink, T. de Rességuier *et al.*, Metals (Basel, Switz.) **6**, 320 (2016).
[6] R. F. Smith *et al.*, J. Appl. Phys. **110**, 123515 (2011).
[7] T. de Rességuier and M. Hallouin, J. Appl. Phys. **84**, 1932 (1998).
[8] D. H. Kalantar, J. F. Belak, G. W. Collins, J. D. Colvin, H. M. Davies, J. H. Eggert, T. C. Germann, J. Hawreliak, B. L. Holian, K. Kadau, P. S. Lomdahl, H. E. Lorenzana, M. A. Meyers, K. Rosolankova, M. S. Schneider, J. Sheppard, J. S. Stölken, and J. S. Wark, Phys. Rev. Lett. **95**, 075502 (2005).
[9] J. Hawreliak, J. D. Colvin, J. H. Eggert, D. H. Kalantar, H. E. Lorenzana, J. S. Stölken, H. M. Davies, T. C. Germann, B. L. Holian, K. Kadau, P. S. Lomdahl, A. Higginbotham,

K. Rosolankova, J. Sheppard, and J. S. Wark, Phys. Rev. B **74**, 184107 (2006).
[10] H. E. Lorenzana *et al.*, Sci. Model. Simul. **15**, 159 (2008).
[11] R. Harrison, A. F. Voter, and S.-P. Chen, in *Atomistic Simulation of Material Plenum* (Plenum, New York, 1989), p. 219.
[12] G. J. Ackland *et al.*, Philos. Mag. A **75**, 713 (1997).
[13] N. Gunkelmann, Eduardo M. Bringa, K. Kang, G. J. Ackland, C. J. Ruestes, and H. M. Urbassek, Phys. Rev. B **86**, 144111 (2012).
[14] K. Wang, S. Xiao, H. Deng, W. Zhu, and W. Hu, Int. J. Plast. **59**, 180 (2014).
[15] K. Kadau, T. C. Germann, P. S. Lomdahl, and B. L. Holian, Science **296**, 1681 (2002).
[16] K. Kadau, T. C. Germann, P. S. Lomdahl, and B. L. Holian, Phys. Rev. B **72**, 064120 (2005).
[17] K. Kadau, T. C. Germann, P. S. Lomdahl, R. C. Albers, J. S. Wark, A. Higginbotham, and B. L. Holian, Phys. Rev. Lett. **98**, 135701 (2007).
[18] W.-W. Pang, P. Zhang, G.-C. Zhang, A.-G. Xu, and X.-G. Zhao, Sci. Rep. **4**, 3628 (2014).
[19] W.-W. Pang, P. Zhang, G.-C. Zhang, A.-G. Xu, and X.-G. Zhao, Sci. Rep. **4**, 5273 (2014).
[20] N. Gunkelmann, E. M. Bringa, D. R. Tramontina, C. J. Ruestes, M. J. Suggit, A. Higginbotham, J. S. Wark, and H. M. Urbassek, Phys. Rev. B **89**, 140102 (2014).
[21] N. Gunkelmann, D. R. Tramontina, E. M. Bringa, and H. M. Urbassek, New J. Phys. **16**, 093032 (2014).
[22] K. Wang, W. Zhu, S. Xiao, K. Chen, H. Deng, and W. Hu, Int. J. Plast. **71**, 218 (2015).
[23] S. Plimpton, J. Comput. Phys. **117**, 1 (1995).
[24] M. S. Daw and M. I. Baskes, Phys. Rev. Lett. **50**, 1285 (1983).
[25] S. M. Foiles, M. I. Baskes, and M. S. Daw, Phys. Rev. B **33**, 7983 (1986).
[26] See LAMMPS Users Manual http://lammps.sandia.gov/doc/Manual.pdf, 22 Feb. 2018, p. 1517.
[27] Chris H. Rycroft, Chaos **19**, 041111 (2009).
[28] A. Paskin, A. Gohar, and G. J. Dienes, J. Phys. Chem. Solids **39**, 1307 (1978).
[29] A. Stukowski, Modell. Simul. Mater. Sci. Eng. **18**, 015012 (2010).
[30] R. Ravelo, T. C. Germann, O. Guerrero, Q. An, and B. L. Holian, Phys. Rev. B **88**, 134101 (2013).
[31] J. N. Johnson and R. W. Rohde, J. Appl. Phys. **42**, 4171 (1971).
[32] M. A. Meyers and L. E. Murr, *Shock Waves and High-Strain-Rate Phenomena in Metals* (Plenum, New York, 1980), p. 487.
[33] J. L. Shao, S. Q. Duan, A. M. He, P. Wang, and C. S. Qin, J. Phys.: Condens. Matter **22**, 355403 (2010).
[34] The LANL equation of state database, 1992.
[35] N. Amadou, E Brambrink, A. Benuzzi-Mounaix, G. Huser, F. Guyot, S. Mazevet, G. Morard, T. de Resseguier *et al.*, High Energy Density Phys. **9**, 243 (2013).
[36] C. E. Wehrenberg *et al.*, Nature (London) **550**, 496 (2017).
[37] R. E. Smallman and A. H. W. Ngan, *Modern Physical Metallurgy* (Elsevier, Oxford, 2014).
[38] D. A. Porter and K. E. Easterling, *Phase Transformations in Metals and Alloys* (Springer, UK, 1992).
[39] J. W. Christian, *The Theory of Transformations in Metals and Alloys* (Elsevier, Oxford, 2002), p. 464.
[40] See Supplementary Material at http://link.aps.org/supplemental/10.1103/PhysRevB.98.024104 for a full animated sequence of wave propagation and material response partially shown in Fig. 4(a).